

# Transport and localization of indirect excitons in a van der Waals heterostructure

L. H. Fowler-Gerace\*,<sup>1</sup> Zhiwen Zhou\*,<sup>1</sup> E. A. Szwed,<sup>1</sup> D.J. Choksy,<sup>1</sup> and L. V. Butov<sup>1</sup>

<sup>1</sup>*Department of Physics, University of California at San Diego, La Jolla, CA 92093, USA*

(Dated: July 1, 2023)

Long lifetimes of spatially indirect excitons (IXs), also known as interlayer excitons, allow implementing both quantum exciton systems and long-range exciton transport. Van der Waals heterostructures (HS) composed of atomically thin layers of transition-metal dichalcogenides (TMD) offer the opportunity to explore IXs in moiré superlattices. The moiré IXs in TMD HS form the materials platform for exploring the Bose-Hubbard physics and superfluid and insulating phases in periodic potentials. IX transport in TMD HS was intensively studied and diffusive IX transport with  $1/e$  decay distances  $d_{1/e}$  up to  $\sim 3 \mu\text{m}$  was realized. In this work, we present in  $\text{MoSe}_2/\text{WSe}_2$  HS the IX long-range transport with  $d_{1/e}$  exceeding  $100 \mu\text{m}$  and diverging at the optical excitation resonant to spatially direct excitons. The IX long-range transport vanishes at high temperatures. With increasing IX density, IX localization, then IX long-range transport, and then IX reentrant localization is observed. The results are in qualitative agreement with the Bose-Hubbard theory of bosons in periodic potentials predicting superfluid at  $N \sim 1/2$  and insulating at  $N \sim 0$  and  $N \sim 1$  phases for the number of bosons per site of the periodic potential  $N$ .

PACS numbers:

A spatially indirect exciton (IX) is a bound pair of an electron and a hole confined in separated layers [1]. Due to the spatial separation of electrons and holes, the lifetimes of IXs can exceed the lifetimes of spatially direct excitons (DXs) by orders of magnitude. The long lifetimes allow IXs to travel long distances. The long-range IX transport has been extensively studied in GaAs HS where the  $1/e$  decay distances of IX luminescence  $d_{1/e}$  reach tens and hundreds of microns [2–17]. The long-range IX transport in GaAs HS enabled the observation of various exciton transport phenomena including the exciton ring [6], the excitonic transistor [8], the exciton delocalization [9], and the coherent exciton transport [12, 17] and spin transport [14, 16].

The temperature of quantum degeneracy, which can be achieved for excitons, scales proportionally to the exciton binding energy  $E_X$  [18]. IXs in GaAs HS have low  $E_X \lesssim 10 \text{ meV}$  [19, 20]. For IXs in III-V and II-VI semiconductor HS, including GaAs [2–17], GaN [21], and ZnO [22] HS, the highest  $E_X \sim 30 \text{ meV}$  is in ZnO HS.

Excitons with remarkably high binding energies can be realized in van der Waals HS composed of atomically thin layers of TMD [23–26]. The IX binding energies in TMD HS reach hundreds of meV [27], making TMD HS the materials platform for the realization of high-temperature IX quantum phenomena [18, 28].

TMD HS offer the opportunity to explore IXs in moiré superlattice potentials with the period  $b \approx a/\sqrt{\delta\theta^2 + \delta^2}$  typically in the  $\sim 10 \text{ nm}$  range ( $a$  is the lattice constant,  $\delta$  the lattice mismatch,  $\delta\theta$  the deviation of the twist angle between the layers from  $i\pi/3$ ,  $i$  is an integer) [29–41]. IXs are out-of-plane dipoles and the interaction between IXs is repulsive [42]. IXs in moiré superlattices provide the experimental realization of the 2D Bose-Hubbard model for bosons with repulsive dipolar interaction.

The moiré potentials can be affected by atomic reconstruction [43, 44] and by disorder. The realization of fairly periodic moiré potentials, in particular on long scales, requires that the disorder is weak.

Transport of both DXs in TMD monolayers (MLs) [45–51] and IXs in TMD HS [52–64] was intensively studied. Diffusive IX transport with  $1/e$  decay distances  $d_{1/e}$  up to a few  $\mu\text{m}$  was realized in these studies. Disordered potentials can be responsible for limiting the IX transport distances in TMD HS. IX transport in TMD HS can be facilitated by voltage-induced suppression of moiré potentials [32, 65] or by moving IXs with acoustic waves [66].

In this work, we present in  $\text{MoSe}_2/\text{WSe}_2$  HS the IX long-range transport with  $d_{1/e}$  exceeding  $100 \mu\text{m}$  and diverging at the optical excitation resonant to DXs. The IX long-range transport vanishes at high temperatures. With increasing IX density, IX localization, then IX long-range transport, and then IX reentrant localization is observed. The results are in qualitative agreement with the Bose-Hubbard theory of bosons in periodic potentials predicting superfluid at  $N \sim 1/2$  and insulating at  $N \sim 0$  and  $N \sim 1$  phases for the number of bosons per site of the periodic potential  $N$  [67].

We study  $\text{MoSe}_2/\text{WSe}_2$  HS assembled by stacking mechanically exfoliated 2D crystals. IXs are formed from electrons and holes confined in adjacent  $\text{MoSe}_2$  and  $\text{WSe}_2$  MLs, respectively, encapsulated by hBN layers. No voltage is applied in the HS. IXs form the lowest-energy exciton state in the  $\text{MoSe}_2/\text{WSe}_2$  HS. The HS details are presented in Supporting Information (SI).

The long-range IX propagation with the diverging decay distance  $d_{1/e}$ , that is with no IX luminescence decay within the entire HS (Fig. 1b), is realized when the optical excitation has the energy  $E_{\text{ex}}$  close to the  $\text{MoSe}_2$  or  $\text{WSe}_2$  DX energy (Fig. 1c). The HS dimensions allow

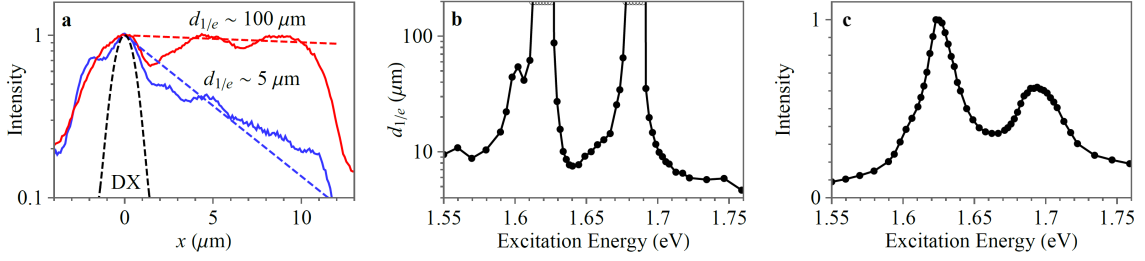


FIG. 1: The long-range IX transport realized with optical excitation resonant to DXs. (a) Normalized IX luminescence profiles for laser excitation off ( $E_{\text{ex}} = 1.771$  eV, blue) and near ( $E_{\text{ex}} = 1.676$  eV, red) the DX absorption resonance. The HS active area extends from  $x = -3$  to  $11$   $\mu\text{m}$ . The blue and red dashed lines show decays with  $d_{1/e} = 5$  and  $100$   $\mu\text{m}$ , respectively. The black dashed line shows the DX luminescence profile in the WSe<sub>2</sub> ML, this profile is close to the laser excitation profile for short-range DX transport. (b) The  $1/e$  decay distance of IX luminescence  $d_{1/e}$  vs.  $E_{\text{ex}}$ .  $d_{1/e}$  are obtained from least-squares fitting the IX luminescence profiles to exponential decays in the region  $x = 0 - 11$   $\mu\text{m}$ . The data with the fit indicating diverging  $d_{1/e}$  are presented by points on the edge. (c) Integrated IX luminescence intensity vs.  $E_{\text{ex}}$  showing two absorption peaks corresponding to the MoSe<sub>2</sub> and WSe<sub>2</sub> DXs.  $P_{\text{ex}} = 0.2$  mW.  $T = 1.7$  K. The  $\sim 1.5$   $\mu\text{m}$  laser spot is centered at  $x = 0$ .

establishing that the longest  $d_{1/e}$  exceed  $100$   $\mu\text{m}$ . In contrast, for a non-resonant excitation,  $d_{1/e}$  is substantially shorter (Fig. 1a,b).

IXs have built-in electric dipoles  $\sim ed_z$  ( $d_z$  is the separation between the electron and hole layers) and the interaction between IXs is repulsive [42]. An enhancement of IX transport with increasing IX density can be caused (i) by the suppression of IX localization and scattering and (ii) by the IX-interaction-induced drift from the origin. The data outlined in the next paragraph show that the first factor, the suppression of IX localization and scattering, causes the major effect.

The nature of the second factor is an increase of IX energy at the excitation spot  $\delta E$  with increasing IX density  $n$  (Fig. 2a) that causes IX drift from the origin [6]. The resonant excitation produces a higher  $n$  due to a higher absorption, thus increasing  $\delta E$  and, in turn, the IX drift. However, the higher  $n$  and  $\delta E$  can be also achieved for nonresonant excitation using higher excitation powers  $P_{\text{ex}}$ . Figure 2b shows  $d_{1/e}$  vs.  $\delta E$  both for the nearly resonant and nonresonant excitation. For the same  $\delta E$ , a significantly higher  $d_{1/e}$  is realized for the (nearly) resonant excitation. This shows that the effect of IX energy increase at the excitation spot on the enhancement of IX transport at resonant excitation is minor and, in turn, that the strong enhancement of IX transport at resonant excitation originates from the suppression of IX localization and scattering. This also shows that the resonant excitation is essential for the realization of the long-range IX transport.

The IX energy increase due to the repulsive interaction  $\delta E$  (Fig. 2a) can be used for estimating the IX density  $n$ . For the long-range IX transport observed at  $P_{\text{ex}} = 0.2$  mW (Figs. 3a, 4a),  $\delta E \sim 3$  meV (Fig. 2) and an estimate for  $n$  using the 'plate capacitor' formula  $\delta E = nu_0$  with  $u_0 = 4\pi e^2 d_z / \epsilon$  [42] gives  $n \sim 2 \times 10^{11}$   $\text{cm}^{-2}$  ( $d_z \sim 0.6$  nm,

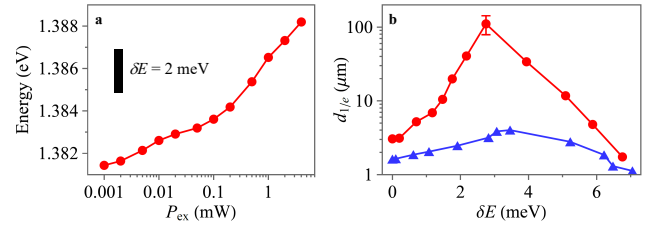


FIG. 2: The IX transport variation with density at resonant and nonresonant excitation. (a) The IX energy at the excitation spot vs.  $P_{\text{ex}}$ .  $E_{\text{ex}} = 1.623$  eV. The scale bar corresponds to the IX energy increase  $\delta E = 2$  meV. (b) The  $1/e$  decay distance of IX luminescence  $d_{1/e}$  vs.  $\delta E$  for resonant ( $E_{\text{ex}} = 1.623$  eV, red) and nonresonant ( $E_{\text{ex}} = 1.96$  eV, blue) excitation.  $T = 6$  K.

the dielectric constant  $\epsilon \sim 7.4$  [68]). The estimated temperature of quantum degeneracy  $T_q = 2\pi\hbar^2 n / (mk_B) \sim 10$  K [18] ( $m \sim 0.9m_0$  is the IX mass in the TMD HS [69]). These estimates indicate that the long-range IX transport is observed at temperatures  $\lesssim T_q$  and at IX densities below the Mott transition density  $n_{\text{Mott}} \gtrsim 10^{12}$   $\text{cm}^{-2}$  [18, 70].

Regarding the role of resonant excitation, heating of the IX system by the excitation close to the DX resonances is, in general, smaller than for non-resonant excitation. In particular, the colder IXs created by the resonant excitation screen the disorder more effectively that can facilitate the emergence of IX superfluidity [6, 9, 71].

IXs in moiré superlattices are repulsively interacting excitons in periodic potentials. For repulsively interacting bosons in periodic potentials, the Bose-Hubbard model predicts both the superfluid phase and insulating phases, such as the Mott insulator and the Bose glass, with the superfluid more stable for the number of particles per lattice site  $N \sim 1/2$  and the insulating for  $N \sim 1$  [67]. The comparison of the data with these predic-

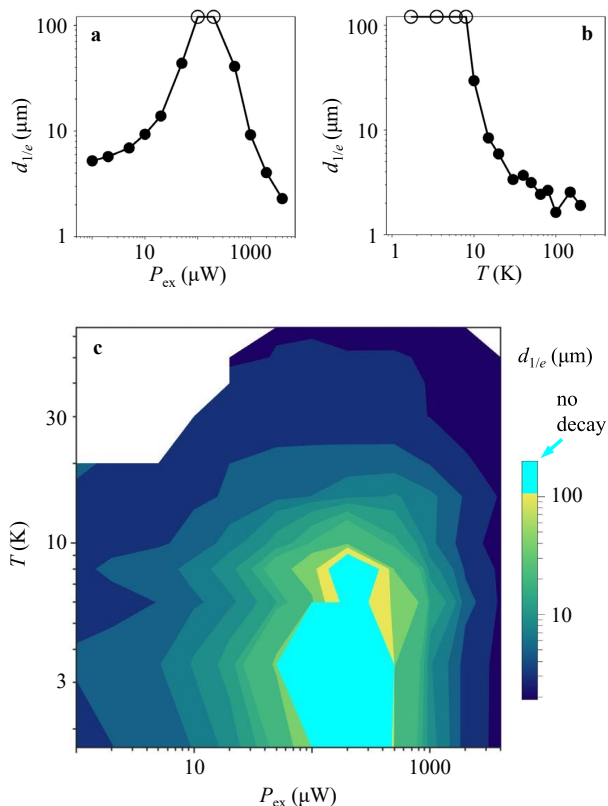


FIG. 3: Excitation power and temperature dependence of IX transport. (a,b) The  $1/e$  decay distance of IX luminescence  $d_{1/e}$  vs.  $P_{\text{ex}}$  (a) and vs. temperature (b). (c)  $d_{1/e}$  vs.  $P_{\text{ex}}$  and temperature.  $d_{1/e}$  are obtained from least-squares fitting the IX luminescence profiles to exponential decays in the region  $x = 0 - 9 \mu\text{m}$ . The data with the fit indicating diverging  $d_{1/e}$  are presented by points on the edge (a,b) or by cyan color (c).  $T = 3.5 \text{ K}$  (a),  $P_{\text{ex}} = 0.2 \text{ mW}$  (b),  $E_{\text{ex}} = 1.689 \text{ eV}$  (a-c).

tions shows that the observed IX transport is consistent with the Bose-Hubbard model for repulsively interacting particles in periodic potentials [67]. (In contrast, the observed IX transport is inconsistent with the classical drift-diffusion model [6] as outlined in SI.)

The variation of IX transport with temperature and excitation power is presented by the variation of  $d_{1/e}$  in Fig. 3a,b. The measured  $P_{\text{ex}} - T$  diagram for the IX transport distance  $d_{1/e}$  is shown in Fig. 3c.

For classical IX drift and diffusion, an in-plane potential suppresses IX transport and a long-range IX transport is observed when the IX interaction energy or thermal energy become comparable to the amplitude of in-plane potential [6, 9]. However, the predicted amplitude of moiré superlattice potential is in the range of tens of meV [29–33] and is much larger than both the interaction energy  $\delta E \sim 3 \text{ meV}$  and thermal energy  $k_B T \lesssim 1 \text{ meV}$  for the observed long-range IX transport. This indicates that the nature of the long-range IX transport is beyond classical drift and diffusion. For IX transport over distances

much larger than the moiré superlattice period, the effect of moiré potential on IX transport is qualitatively similar for R and H (AA and AB) stacking: Both for R and H stacking, IXs propagate in a periodic moiré potential with the period  $b \sim a/\delta\theta$  and large amplitude. The values for the latter for R and H stacking are  $E_R \sim 100 \text{ meV}$  and  $E_H \sim 25 \text{ meV}$  [29–33]. Since both  $E_R$  and  $E_H$  are much larger than  $\delta E$  and  $k_B T$ , the discussions of IX transport apply to both R and H stacking.

The suppression of IX transport with density is observed at high densities (Fig. 3a). This is also inconsistent with classical IX drift and diffusion. For classical IX drift and diffusion, the density dependence is the opposite: both the IX diffusion coefficient and the IX drift increase with density, the former due to the enhanced screening of in-plane potential and the latter due to the enhanced  $\delta E$  at the origin [6, 9], as outlined in SI. An enhancement of IX transport with density due to these factors is observed for IXs in both GaAs and TMD HS [6, 9, 53, 61, 63]. In contrast, the reentrant localization of IXs at densities higher than the reentrants corresponding to the long-range transport of IXs (Fig. 3a) is observed for IXs in TMD HS with periodic moiré potential.

The observed enhancement followed by the suppression of IX transport with density (Fig. 3a) is in agreement with the predictions of the Bose-Hubbard model for quantum transport of bosons in periodic potentials. The number of IXs per site of the moiré superlattice  $N$  increases with density. For the maximum IX transport distances (Figs. 2, 3a), the IX density  $n$  estimated from the energy shift  $\delta E = nu_0$  [42] as outlined above is  $\sim 2 \times 10^{11} \text{ cm}^{-2}$ .  $N \sim 1/2$  at  $n \sim 2 \times 10^{11} \text{ cm}^{-2}$  for the superlattice period  $b = 17 \text{ nm}$ . This period  $b \sim a/\delta\theta$  corresponds to the twist angle  $\delta\theta = 1.1^\circ$ , which agrees with the angle between  $\text{MoSe}_2$  and  $\text{WSe}_2$  edges in the HS (Fig. S2c), see SI. The IX transport is suppressed for the higher  $P_{\text{ex}}$  realizing the higher  $\delta E$ ,  $n$ , and  $N$  (Figs. 2, 3a). This estimate indicates that the IX long-range transport and localization are in qualitative agreement with the Bose-Hubbard theory of bosons in periodic potentials predicting superfluid at  $N \sim 1/2$  and insulating at  $N \sim 0$  and  $N \sim 1$  phases for the number of bosons per site of the periodic potential  $N$ .

The IX long-range transport with the diverging decay distance vanishes at  $T \sim 10 \text{ K}$  (Fig. 3b). This is in qualitative agreement with the transition to a non-superfluid phase with increasing temperature [67]. (In contrast, for the classical diffusive IX transport [6], the temperature dependence is the opposite: the IX diffusion increases with temperature, as outlined in SI.)

The theory predicts that the critical temperature for the superfluid-normal transition for bosons in periodic potentials  $T_c \sim 4\pi NJ$  [72]. The inter-site hopping  $J$  is determined by the lattice parameters and drops with increasing lattice amplitude  $E_1$ .  $T_c \sim 10 \text{ K}$  corresponds to  $J \sim 1.6 \text{ K}$  [72] and, in turn, for the moiré potential with

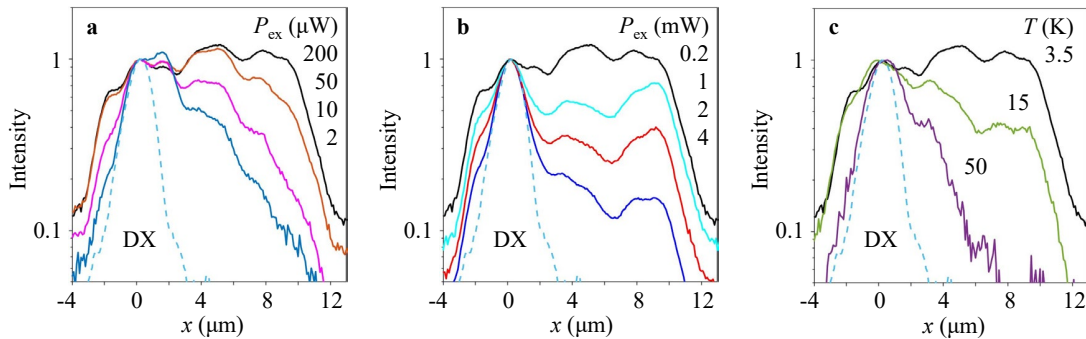


FIG. 4: Excitation power and temperature dependence of IX transport. (a-c) Normalized IX luminescence profiles for different  $P_{\text{ex}}$  (a,b) and temperatures (c). The dashed line shows the DX luminescence profile in the MoSe<sub>2</sub> ML, this profile is close to the laser excitation profile for short-range DX transport.  $T = 3.5$  K (a,b),  $P_{\text{ex}} = 0.2$  mW (c),  $E_{\text{ex}} = 1.689$  eV (a-c). The  $\sim 2$   $\mu\text{m}$  laser spot is centered at  $x = 0$ .

$b \sim 17$  nm, to  $E_1 \sim 8$  meV [73]. This value is smaller than the amplitudes considered in Refs. [29–33]. However, the estimates here are rough and developing the theory of IX superfluidity in moiré potentials is needed for a more accurate comparison.

The theory predicts that higher  $T_c$  can be achieved in lattices with higher  $J$  [72]. This can be realized in moiré superlattices with smaller periods in HS with larger twist angles between the TMD layers.

The theory also predicts that at  $N \sim 1$ , the Mott insulator form for sufficiently high on-site interaction  $U$  ( $U \gtrsim 17$ ) [72]. For the considered moiré superlattice, the estimated  $U \gtrsim 10$  meV exceeds the required value and the insulating phase should form at  $N \sim 1$  according to the theory. This is in agreement with IX localization at  $N \sim 1$  observed in the experiment.

In summary, this work presents in a MoSe<sub>2</sub>/WSe<sub>2</sub> HS the IX long-range transport with the decay distance  $d_{1/e}$  exceeding  $100$   $\mu\text{m}$  and diverging at the optical excitation resonant to DXs. The IX long-range transport vanishes at temperatures  $\gtrsim 10$  K. With increasing IX density, IX localization, then IX long-range transport, and then IX reentrant localization is observed. The results are in qualitative agreement with the Bose-Hubbard theory of bosons in periodic potentials predicting superfluid at  $N \sim 1/2$  and insulating at  $N \sim 0$  and  $N \sim 1$  phases for the number of bosons per site of the periodic potential  $N$ .

#### ACKNOWLEDGMENTS

We thank M.M. Fogler and J.R. Leonard for discussions. We especially thank A.H. MacDonald for discussions of IXs in moiré potentials and A.K. Geim for teaching us manufacturing TMD HS. The studies were supported by DOE Office of Basic Energy Sciences under Award DE-FG02-07ER46449. The HS manufacturing

was supported by NSF Grant 1905478.

\*equal contribution

#### References

- [1] Y.E. Lozovik, V.I. Yudson, A new mechanism for superconductivity: pairing between spatially separated electrons and holes, *Sov. Phys. JETP* **44**, 389 (1976).
- [2] M. Hagn, A. Zrenner, G. Böhm, G. Weimann, Electric-field-induced exciton transport in coupled quantum well structures, *Appl. Phys. Lett.* **67**, 232 (1995).
- [3] A.V. Larionov, V.B. Timofeev, J. Hvam, K. Soerensen, Interwell Excitons in GaAs/AlGaAs Double Quantum Wells and Their Collective Properties, *J. Exp. Theor. Phys.* **90**, 1093 (2000).
- [4] L.V. Butov, A.C. Gossard, D.S. Chemla, Macroscopically ordered state in an exciton system, *Nature* **418**, 751 (2002).
- [5] Z. Vörös, R. Balili, D.W. Snoke, L. Pfeiffer, K. West, Long-Distance Diffusion of Excitons in Double Quantum Well Structures, *Phys. Rev. Lett.* **94**, 226401 (2005).
- [6] A.L. Ivanov, L.E. Smallwood, A.T. Hammack, Sen Yang, L.V. Butov, A.C. Gossard, Origin of the inner ring in photoluminescence patterns of quantum well excitons, *Europhys. Lett.* **73**, 920 (2006).
- [7] A. Gärtner, A.W. Holleitner, J.P. Kotthaus, D. Schuh, Drift mobility of long-living excitons in coupled GaAs quantum wells, *Appl. Phys. Lett.* **89**, 052108 (2006).
- [8] A.A. High, E.E. Novitskaya, L.V. Butov, M. Hanson, A.C. Gossard, Control of exciton fluxes in an excitonic integrated circuit, *Science* **321**, 229 (2008).
- [9] M. Remeika, J.C. Graves, A.T. Hammack, A.D. Meyert-holen, M.M. Fogler, L.V. Butov, M. Hanson and A.C. Gossard, Localization-Delocalization Transition of Indirect Excitons in Lateral Electrostatic Lattices, *Phys. Rev. Lett.* **102**, 186803 (2009).

- [10] X.P. Vögele, D. Schuh, W. Wegscheider, J.P. Kotthaus, A.W. Holleitner, Density Enhanced Diffusion of Dipolar Excitons within a One-Dimensional Channel, *Phys. Rev. Lett.* **103**, 126402 (2009).
- [11] S. Lazić, P.V. Santos, R. Hey, Exciton transport by moving strain dots in GaAs quantum wells, *Phys. E* **42**, 2640 (2010).
- [12] A.A. High, J.R. Leonard, A.T. Hammack, M.M. Fogler, L.V. Butov, A.V. Kavokin, K.L. Campman, A.C. Gossard, Spontaneous coherence in a cold exciton gas, *Nature* **483**, 584 (2012).
- [13] M. Alloing, A. Lemaître, E. Galopin, F. Dubin, Nonlinear dynamics and inner-ring photoluminescence pattern of indirect excitons, *Phys. Rev. B* **85**, 245106 (2012).
- [14] A.A. High, A.T. Hammack, J.R. Leonard, Sen Yang, L.V. Butov, T. Ostatnický, M. Vladimirova, A.V. Kavokin, T.C.H. Liew, K.L. Campman, A.C. Gossard, Spin Currents in a Coherent Exciton Gas, *Phys. Rev. Lett.* **110**, 246403 (2013).
- [15] S. Lazić, A. Violante, K. Cohen, R. Hey, R. Rapaport, P.V. Santos, Scalable interconnections for remote indirect exciton systems based on acoustic transport, *Phys. Rev. B* **89**, 085313 (2014).
- [16] J.R. Leonard, A.A. High, A.T. Hammack, M.M. Fogler, L.V. Butov, K.L. Campman, A.C. Gossard, Pancharatnam-Berry phase in condensate of indirect excitons, *Nat. Commun.* **9**, 2158 (2018).
- [17] J.R. Leonard, Lunhui Hu, A.A. High, A.T. Hammack, Congjun Wu, L.V. Butov, K.L. Campman, A.C. Gossard, Moiré pattern of interference dislocations in condensate of indirect excitons, *Nat. Commun.* **12**, 1175 (2021).
- [18] M.M. Fogler, L.V. Butov, K.S. Novoselov, High-temperature superfluidity with indirect excitons in van der Waals heterostructures, *Nature Commun.* **5**, 4555 (2014).
- [19] A. Zrenner, P. Leeb, J. Schäfler, G. Böhm, G. Weimann, J.M. Worlock, L.T. Florez, J.P. Harbison, Indirect excitons in coupled quantum well structures, *Surf. Sci.* **263**, 496 (1992).
- [20] K. Sivalertporn, L. Mouchliadis, A.L. Ivanov, R. Philp, E.A. Muljarov, Direct and indirect excitons in semiconductor coupled quantum wells in an applied electric field, *Phys. Rev. B* **85**, 045207 (2012).
- [21] François Chiaruttini, Thierry Guillet, Christelle Brimont, Benoit Jouault, Pierre Lefebvre, Jessica Vives, Sebastien Chenot, Yvon Cordier, Benjamin Damilano, Maria Vladimirova, Trapping Dipolar Exciton Fluids in GaN/(AlGa)N Nanostructures, *Nano Lett.* **19**, 4911 (2019).
- [22] C. Morhain, T. Bretagnon, P. Lefebvre, X. Tang, P. Valvin, T. Guillet, B. Gil, T. Taliercio, M. Teisseire-Doninelli, B. Vinter, C. Deparis, Internal electric field in wurtzite ZnO/Zn<sub>0.78</sub>Mg<sub>0.22</sub>O quantum wells, *Phys. Rev. B* **72**, 241305(R) (2005).
- [23] A.K. Geim, I.V. Grigorieva, Van der Waals heterostructures, *Nature* **499**, 419 (2013).
- [24] Ziliang Ye, Ting Cao, Kevin O'Brien, Hanyu Zhu, Xiaobo Yin, Yuan Wang, Steven G. Louie, Xiang Zhang, Probing excitonic dark states in single-layer tungsten disulphide, *Nature* **513**, 214 (2014).
- [25] Alexey Chernikov, Timothy C. Berkelbach, Heather M. Hill, Albert Rigosi, Yilei Li, Ozgur Burak Aslan, David R. Reichman, Mark S. Hybertsen, Tony F. Heinz, Exciton Binding Energy and Nonhydrogenic Rydberg Series in Monolayer WS<sub>2</sub>, *Phys. Rev. Lett.* **113**, 076802 (2014).
- [26] M. Goryca, J. Li, A.V. Stier, T. Taniguchi, K. Watanabe, E. Courtade, S. Shree, C. Robert, B. Urbaszek, X. Marie, S.A. Crooker, Revealing exciton masses and dielectric properties of monolayer semiconductors with high magnetic fields, *Nature Commun.* **10**, 4172 (2019).
- [27] Thorsten Deilmann, Kristian Sommer Thygesen, Interlayer Trions in the MoS<sub>2</sub>/WS<sub>2</sub> van der Waals Heterostructure, *Nano Lett.* **18**, 1460 (2018).
- [28] Oleg L. Berman, Roman Ya. Kezerashvili, Superfluidity of dipolar excitons in a transition metal dichalcogenide double layer, *Phys. Rev. B* **96**, 094502 (2017).
- [29] Fengcheng Wu, Timothy Lovorn, A.H. MacDonald, Theory of optical absorption by interlayer excitons in transition metal dichalcogenide heterobilayers, *Phys. Rev. B* **97**, 035306 (2018).
- [30] Hongyi Yu, Gui-Bin Liu, Wang Yao, Brightened spin-triplet interlayer excitons and optical selection rules in van der Waals heterobilayers, *2D Mater.* **5**, 035021 (2018).
- [31] Fengcheng Wu, Timothy Lovorn, A.H. MacDonald, Topological Exciton Bands in Moiré Heterojunctions, *Phys. Rev. Lett.* **118**, 147401 (2017).
- [32] Hongyi Yu, Gui-Bin Liu, Jianju Tang, Xiaodong Xu, Wang Yao, Moiré excitons: From programmable quantum emitter arrays to spin-orbit-coupled artificial lattices, *Sci. Adv.* **3**, e1701696 (2017).
- [33] Chendong Zhang, Chih-Piao Chuu, Xibiao Ren, Ming-Yang Li, Lain-Jong Li, Chuanhong Jin, Mei-Yin Chou, Chih-Kang Shih, Interlayer couplings, Moiré patterns, and 2D electronic superlattices in MoS<sub>2</sub>/WSe<sub>2</sub> hetero-bilayers, *Sci. Adv.* **3**, e1601459 (2017).
- [34] Pasqual Rivera, Hongyi Yu, Kyle L. Seyler, Nathan P. Wilson, Wang Yao, Xiaodong Xu, Interlayer valley excitons in heterobilayers of transition metal dichalcogenides, *Nature Nano.* **13**, 1004 (2018).
- [35] Kyle L. Seyler, Pasqual Rivera, Hongyi Yu, Nathan P. Wilson, Essance L. Ray, David G. Mandrus, Jiaqiang Yan, Wang Yao, Xiaodong Xu, Signatures of moiré-trapped valley excitons in MoSe<sub>2</sub>/WSe<sub>2</sub> heterobilayers, *Nature* **567**, 66 (2019).
- [36] Kha Tran, Galan Moody, Fengcheng Wu, Xiaobo Lu, Junho Choi, Kyoungwan Kim, Amritesh Rai, Daniel A. Sanchez, Jiamin Quan, Akshay Singh, Jacob Embley, André Zepeda, Marshall Campbell, Travis Autry, Takashi Taniguchi, Kenji Watanabe, Nanshu Lu, Sanjay K. Banerjee, Kevin L. Silverman, Suenne Kim, Emanuel Tutuc, Li Yang, Allan H. MacDonald, Xiaoqin Li, Evidence for moiré excitons in van der Waals heterostructures, *Nature* **567**, 71 (2019).
- [37] Chenhao Jin, Emma C. Regan, Aiming Yan, M. Iqbal Bakti Utama, Danqing Wang, Sihan Zhao, Ying Qin, Sijie Yang, Zhiren Zheng, Shenyang Shi, Kenji Watanabe, Takashi Taniguchi, Sefaattin Tongay, Alex Zettl, Feng Wang, Observation of moiré excitons in WSe<sub>2</sub>/WS<sub>2</sub> heterostructure superlattices, *Nature* **567**, 76 (2019).
- [38] Evgeny M. Alexeev, David A. Ruiz-Tijerina, Mark Danovich, Matthew J. Hamer, Daniel J. Terry, Pramoda K. Nayak, Seongjoon Ahn, Sangyeon Pak, Juwon Lee, Jung Inn Sohn, Maciej R. Molas, Maciej Koperski, Kenji Watanabe, Takashi Taniguchi, Kostya S. Novoselov, Roman V. Gorbachev, Hyeon Suk Shin, Vladimir I. Fal'ko, Alexander I. Tartakovskii, Resonantly hybridized excitons in moiré superlattices in van der Waals heterostructures, *Nature* **567**, 81 (2019).
- [39] Yuya Shimazaki, Ido Schwartz, Kenji Watanabe, Takashi Taniguchi, Martin Kroner, Ataç Imamoğlu, Strongly correlated electrons and hybrid excitons in a moiré heterostructure



- ture, *Nature* **580**, 472 (2020).
- [40] Nathan P. Wilson, Wang Yao, Jie Shan, Xiaodong Xu, Excitons and emergent quantum phenomena in stacked 2D semiconductors, *Nature* **599**, 383 (2021).
- [41] Jie Gu, Liguang Ma, Song Liu, Kenji Watanabe, Takashi Taniguchi, James C. Hone, Jie Shan, Kin Fai Mak, Dipolar excitonic insulator in a moiré lattice, *Nature Physics* **18**, 395 (2022).
- [42] D. Yoshioka, A.H. MacDonald, Double quantum well electron-hole systems in strong magnetic fields, *J. Phys. Soc. Jpn.* **59**, 4211 (1990).
- [43] Astrid Weston, Yichao Zou, Vladimir Enaldiev, Alex Summerfield, Nicholas Clark, Viktor Zólyomi, Abigail Graham, Celal Yelgel, Samuel Magorrian, Mingwei Zhou, Johanna Zultak, David Hopkinson, Alexei Barinov, Thomas H. Bointon, Andrey Kretinin, Neil R. Wilson, Peter H. Beton, Vladimir I. Fal'ko, Sarah J. Haigh, and Roman Gorbachev, Atomic reconstruction in twisted bilayers of transition metal dichalcogenides, *Nature Nano.* **15**, 592 (2020).
- [44] Matthew R. Rosenberger, Hsun-Jen Chuang, Madeleine Phillips, Vladimir P. Oleshko, Kathleen M. McCreary, Saujan V. Sivaram, C. Stephen Hellberg, and Berend T. Jonker, Twist Angle-Dependent Atomic Reconstruction and Moiré Patterns in Transition Metal Dichalcogenide Heterostructures, *ACS Nano* **14**, 4550 (2020).
- [45] Nardeep Kumar, Qiannan Cui, Frank Ceballos, Dawei He, Yongsheng Wang, Hui Zhao, Exciton diffusion in monolayer and bulk MoSe<sub>2</sub>, *Nanoscale* **6**, 4915, (2014).
- [46] Marvin Kulig, Jonas Zipfel, Philipp Nagler, Sofia Blanter, Christian Schüller, Tobias Korn, Nicola Paradiso, Mikhail M. Glazov, Alexey Chernikov, Exciton Diffusion and Halo Effects in Monolayer Semiconductors, *Phys. Rev. Lett.* **120**, 207401 (2018).
- [47] F. Cadiz, C. Robert, E. Courtade, M. Manca, L. Martinelli, T. Taniguchi, K. Watanabe, T. Amand, A.C.H. Rowe, D. Paget, B. Urbaszek, X. Marie, Exciton diffusion in WSe<sub>2</sub> monolayers embedded in a van der Waals heterostructure, *Appl. Phys. Lett.* **112**, 152106 (2018).
- [48] Darwin F. Cordovilla Leon, Zidong Li, Sung Woon Jang, Che-Hsuan Cheng, Parag B. Deotare, Exciton transport in strained monolayer WSe<sub>2</sub>, *Appl. Phys. Lett.* **113**, 252101 (2018).
- [49] Darwin F. Cordovilla Leon, Zidong Li, Sung Woon Jang, Parag B. Deotare, Hot exciton transport in WSe<sub>2</sub> monolayers, *Phys. Rev. B* **100**, 241401(R) (2019).
- [50] Shengcai Hao, Matthew Z. Bellus, Dawei He, Yongsheng Wang, Hui Zhao, Controlling exciton transport in monolayer MoSe<sub>2</sub> by dielectric screening, *Nanoscale Horiz.* **5**, 139 (2020).
- [51] Kanak Datta, Zhengyang Lyu, Zidong Li, Takashi Taniguchi, Kenji Watanabe, Parag B. Deotare, Spatiotemporally controlled room-temperature exciton transport under dynamic strain, *Nature Photonics* **16**, 242 (2022).
- [52] Pasqual Rivera, Kyle L. Seyler, Hongyi Yu, John R. Schaibley, Jiaqiang Yan, David G. Mandrus, Wang Yao, Xiaodong Xu, Valley-polarized exciton dynamics in a 2D semiconductor heterostructure, *Science* **351**, 688 (2016).
- [53] Luis A. Jauregui, Andrew Y. Joe, Kateryna Pistunova, Dominik S. Wild, Alexander A. High, You Zhou, Giovanni Scuri, Kristiaan De Greve, Andrey Sushko, Che-Hang Yu, Takashi Taniguchi, Kenji Watanabe, Daniel J. Needleman, Mikhail D. Lukin, Hongkun Park, Philip Kim, Electrical control of interlayer exciton dynamics in atomically thin heterostructures, *Science* **366**, 870 (2019).
- [54] Dmitrii Unuchek, Alberto Ciarrocchi, Ahmet Avsar, Kenji Watanabe, Takashi Taniguchi, Andras Kis, Room-temperature electrical control of exciton flux in a van der Waals heterostructure, *Nature* **560**, 340 (2019).
- [55] Dmitrii Unuchek, Alberto Ciarrocchi, Ahmet Avsar, Zhe Sun, Kenji Watanabe, Takashi Taniguchi, Andras Kis, Valley-polarized exciton currents in a van der Waals heterostructure, *Nature Nanotechnology* **14**, 1104 (2019).
- [56] Yuanda Liu, Kevin Dini, Qinghai Tan, Timothy Liew, Kostya S. Novoselov, Weibo Gao, Electrically controllable router of interlayer excitons, *Sci. Adv.* **6**, eaba1830 (2020).
- [57] Junho Choi, Wei-Ting Hsu, Li-Syuan Lu, Liuyang Sun, Hui-Yu Cheng, Ming-Hao Lee, Jiamin Quan, Kha Tran, Chun-Yuan Wang, Matthew Staab, Kayleigh Jones, Takashi Taniguchi, Kenji Watanabe, Ming-Wen Chu, Shangjr Gwo, Suenne Kim, Chih-Kang Shih, Xiaoqin Li, Wen-Hao Chang, Moiré potential impedes interlayer exciton diffusion in van der Waals heterostructures, *Sci. Adv.* **6**, eaba8866 (2020).
- [58] Zumeng Huang, Yuanda Liu, Kevin Dini, Qinghai Tan, Zhuojun Liu, Hanlin Fang, Jin Liu, Timothy Liew, Weibo Gao, Robust room temperature valley Hall effect of interlayer excitons, *Nano Lett.* **20**, 1345 (2020).
- [59] Long Yuan, Biyuan Zheng, Jens Kunstmann, Thomas Brumme, Agnieszka Beata Kuc, Chao Ma, Shibin Deng, Daria Blach, Anlian Pan, Libai Huang, Twist-angle-dependent interlayer exciton diffusion in WS<sub>2</sub>-WSe<sub>2</sub> heterobilayers, *Nat. Mat.* **19**, 617 (2020).
- [60] Zidong Li, Xiaobo Lu, Darwin F. Cordovilla Leon, Zhengyang Lyu, Hongchao Xie, Jize Hou, Yanzhao Lu, Xiaoyu Guo, Austin Kaczmarek, Takashi Taniguchi, Kenji Watanabe, Liuyan Zhao, Li Yang, Parag B. Deotare, Interlayer Exciton Transport in MoSe<sub>2</sub>/WSe<sub>2</sub> Heterostructures, *ACS Nano* **15**, 1539 (2021).
- [61] Jue Wang, Qianhui Shi, En-Min Shih, Lin Zhou, Wenjing Wu, Yusong Bai, Daniel Rhodes, Katayun Barmak, James Hone, Cory R. Dean, X.-Y. Zhu, Diffusivity Reveals Three Distinct Phases of Interlayer Excitons in MoSe<sub>2</sub>/WSe<sub>2</sub> Heterobilayers, *Phys. Rev. Lett.* **126**, 106804 (2021).
- [62] Daniel N. Shanks, Fateme Mahdikhanyarvejahany, Trevor G. Stanfill, Michael R. Koehler, David G. Mandrus, Takashi Taniguchi, Kenji Watanabe, Brian J. LeRoy, John R. Schaibley, Interlayer Exciton Diode and Transistor, *Nano Lett.* **22**, 6599 (2022).
- [63] Zhe Sun, Alberto Ciarrocchi, Fedele Tagarelli, Juan Francisco Gonzalez Marin, Kenji Watanabe, Takashi Taniguchi, Andras Kis, Excitonic transport driven by repulsive dipolar interaction in a van der Waals heterostructure, *Nature Photonics* **16**, 79 (2022).
- [64] Fedele Tagarelli, Edoardo Lopriore, Daniel Erkensten, Raúl Perea-Causín, Samuel Brem, Joakim Hagel, Zhe Sun, Gabriele Pasquale, Kenji Watanabe, Takashi Taniguchi, Ermin Malic, Andras Kis, Electrical control of hybrid exciton transport in a van der Waals heterostructure, *Nature Photonics*, <https://doi.org/10.1038/s41566-023-01198-w> (2023).
- [65] L.H. Fowler-Gerace, D.J. Choksy, L.V. Butov, Voltage-controlled long-range propagation of indirect excitons in a van der Waals heterostructure, *Phys. Rev. B* **104**, 165302 (2021).
- [66] Ruoming Peng, Adina Ripin, Yusen Ye, Jiayi Zhu, Changming Wu, Seokhyeong Lee, Huan Li, Takashi Taniguchi, Kenji Watanabe, Ting Cao, Xiaodong Xu, Mo Li, Long-range transport of 2D excitons with acoustic waves, *Nat. Commun.* **13**, 1334 (2022).

- [67] Matthew P. A. Fisher, Peter B. Weichman, G. Grinstein, Daniel S. Fisher, Boson localization and the superfluid-insulator transition, *Phys. Rev. B* **40**, 546 (1989).
- [68] Akash Laturia, Maarten L. Van de Put, William G. Vandenberghe, Dielectric properties of hexagonal boron nitride and transition metal dichalcogenides: from monolayer to bulk, *2D Materials and Applications* **2**, 6 (2018).
- [69] Andor Kormányos, Guido Burkard, Martin Gmitra, Jaroslav Fabian, Viktor Zólyomi, Neil D. Drummond, Vladimir Fal'ko,  $\mathbf{k}\text{-p}$  theory for two-dimensional transition metal dichalcogenide semiconductors, *2D Mater.* **2**, 049501 (2015).
- [70] Jue Wang, Jenny Ardelean, Yusong Bai, Alexander Steinhoff, Matthias Florian, Frank Jahnke, Xiaodong Xu, Mackillo Kira, James Hone, X.-Y. Zhu, Optical generation of high carrier densities in 2D semiconductor heterobilayers, *Sci. Adv.* **5**, eaax0145 (2019).
- [71] Dmitri E. Nikonov, Atac Imamoglu, Bose condensation in two dimensions with disorder: Gross-Pitaevskii approach, arXiv:quant-ph/9806003 (1998).
- [72] Barbara Capogrosso-Sansone, Şebnem Güneş Söyler, Nikolay Prokof'ev, Boris Svistunov, Monte Carlo study of the two-dimensional Bose-Hubbard model, *Phys. Rev. A* **77**, 015602 (2008).
- [73] M. Remeika, M.M. Fogler, L.V. Butov, M. Hanson, A.C. Gossard, Two-dimensional electrostatic lattices for indirect excitons, *Appl. Phys. Lett.* **100**, 061103 (2012).

# Supporting Information for Transport and localization of indirect excitons in a van der Waals heterostructure

L. H. Fowler-Gerace\*,<sup>1</sup> Zhiwen Zhou\*,<sup>1</sup> E. A. Szwed,<sup>1</sup> D.J. Choksy,<sup>1</sup> and L. V. Butov<sup>1</sup>

<sup>1</sup>Department of Physics, University of California at San Diego, La Jolla, CA 92093, USA

(Dated: July 1, 2023)

PACS numbers:

## Supplementary Notes 1: The heterostructure details

The van der Waals heterostructure was assembled using the dry-transfer peel-and-lift technique [1]. Crystals of hBN, MoSe<sub>2</sub>, and WSe<sub>2</sub> were first mechanically exfoliated onto different Si substrates that were coated with a double polymer layer consisting of polymethyl glutarimide (PMGI) and polymethyl methacrylate (PMMA). The bottom PMGI was then dissolved with the tetramethylammonium hydroxide based solvent CD-26, causing the top PMMA membrane with the target 2D crystal to float on top of the solvent. The PMMA membrane functions both as a support substrate for transferring the crystal and as a barrier to protect the crystal from the solvent. Separately, a large graphite crystal was exfoliated onto an oxidized Si wafer, which served as the basis for the heterostructure. The PMMA membrane supporting the target crystal was then flipped over and aligned above a flat region of the graphite crystal using a micromechanical transfer stage. The two crystals were brought into contact and the temperature of the stage was ramped to 80° C in order to increase adhesion between the 2D crystals. Then, the PMMA membrane was peeled off leaving the bilayer stack on the wafer. The procedure was repeated leading to a multicrystal stack with the desired layer sequence. Sample annealing was performed by immersing the sample in Remover PG, an N-methyl-2-pyrrolidone (NMP) based solvent stripper, at 70° C for 12 hours.

No intentional sample doping was done; however, unintentional *n*-type doping is typical for TMD layers [1]. The thickness of bottom and top hBN layers is about 40 and 30 nm, respectively. The MoSe<sub>2</sub> layer is on top of the WSe<sub>2</sub> layer. The long WSe<sub>2</sub> and MoSe<sub>2</sub> edges reach ~ 30 and ~ 20 μm, respectively, which enables a rotational alignment between the WSe<sub>2</sub> and MoSe<sub>2</sub> monolayers. The twist angle  $\delta\theta = 1.1^\circ$  corresponding to the moiré superlattice period  $b = 17$  nm, which gives  $N \sim 1/2$  at the estimated  $n \sim 2 \times 10^{11}$  cm<sup>-2</sup> for the long-range IX transport as outlined in the main text, agrees with the angle between MoSe<sub>2</sub> and WSe<sub>2</sub> edges in the HS (Fig. S2c).

The accuracies of estimating  $\delta\theta$  using the long WSe<sub>2</sub> and MoSe<sub>2</sub> edges and using SHG are comparable. We do not use SHG for additional estimates of  $\delta\theta$  since the intense optical excitation pulses in SHG measurements may cause

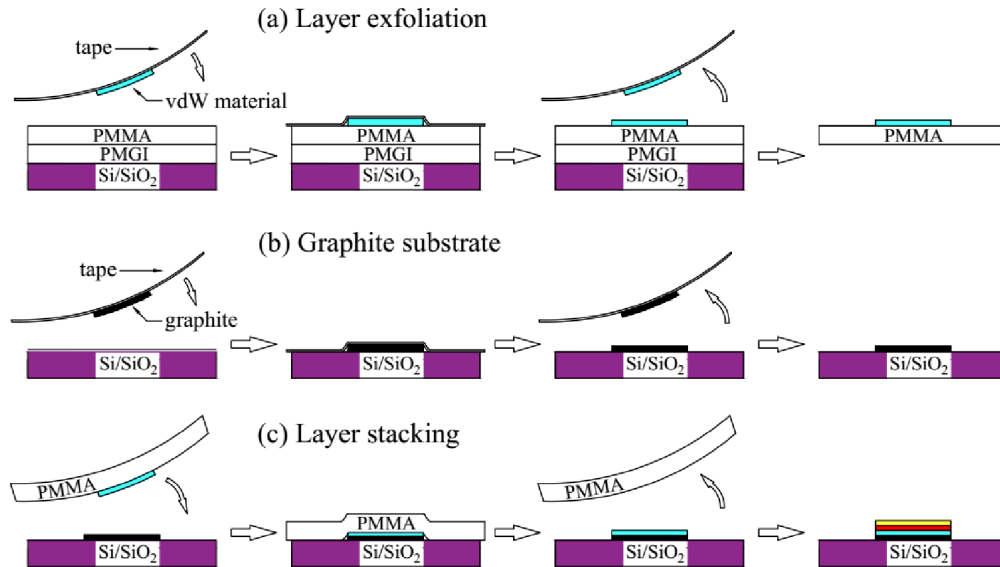


FIG. S1: Sample fabrication process. (a) Van der Waals layer exfoliation. (b) Graphite substrate exfoliation. (c) Layer stacking.



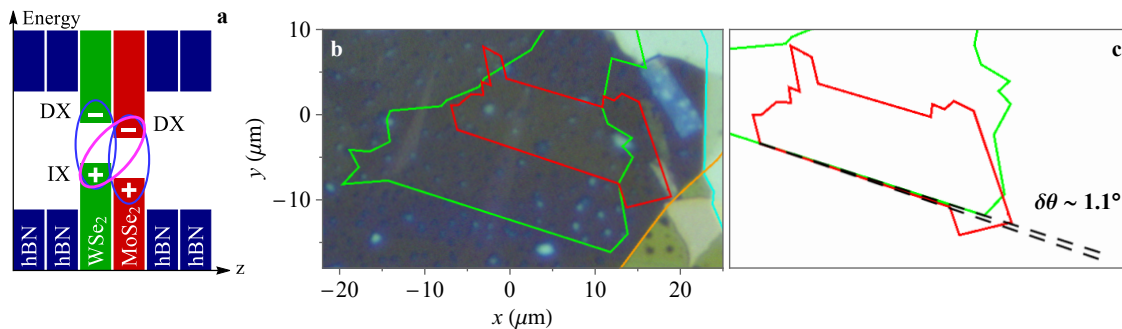


FIG. S2: (a) Schematic energy-band diagram for the HS. The ovals indicate a direct exciton (DX) and an indirect exciton (IX) composed of an electron (-) and a hole (+). (b) A microscope image showing the layer pattern of the HS. The green, red, cyan, and orange lines indicate the boundaries of WSe<sub>2</sub> and MoSe<sub>2</sub> monolayers and bottom and top hBN layers, respectively. (c) A schematic showing the angle between MoSe<sub>2</sub> and WSe<sub>2</sub> edges in the HS. The layers contours are shifted keeping their orientation. The angle between MoSe<sub>2</sub> and WSe<sub>2</sub> edges in the HS is compared with  $\delta\theta = 1.1^\circ$  (the angle between the dashed lines).

a deterioration of the HS and may suppress the long-range IX transport. We note that  $\delta\theta$  and, in turn, the moiré potential may vary over the HS area.

Figure S2 presents a microscope image showing the layer pattern of the HS. The layer boundaries are indicated. The hBN layers cover the entire areas of MoSe<sub>2</sub> and WSe<sub>2</sub> layers. There was a narrow multilayer graphene electrode on the top of the HS around  $x = 2 \mu\text{m}$  for  $y = 0$ , Fig. S2. This electrode was detached. The IX luminescence reduction around  $x = 2 \mu\text{m}$  can be related with residual graphene layers on the HS.

The discussions of IX transport and localization in this work apply to both R and H (AA and AB) stacking: the predicted amplitude of moiré superlattice potential for MoSe<sub>2</sub>/WSe<sub>2</sub> HS with R and H stacking is  $\sim 100$  and  $\sim 25$  meV, respectively [2, 3] and both these values are much larger than the interaction energy  $\delta E \sim 3$  meV and thermal energy  $k_B T \lesssim 1$  meV for the observed long-range IX transport. We did not verify if stacking in the sample is R or H. As outlined in the main text, the observed IX transport phenomena are qualitatively similar for R and H stacking. It is important to verify the role of the rotational alignment between the HS layers on the IX localization and transport. So far the long-range IX transport with the decay distance  $d_{1/e}$  exceeding  $100 \mu\text{m}$  was realized in one sample in this work. Other samples show  $d_{1/e}$  up to a few  $\mu\text{m}$  [4–16]. The shorter range of IX transport likely originates from disorder, which suppresses conducting phases [17]. The sample studied in this work demonstrates the existence of the IX long-range transport and reentrant localization and allows measuring the density-temperature phase diagram for these phenomena and comparing it with the theory. However, it is essential to study these phenomena in other samples and, in particular, to study the dependence on the twist angle. The sample statistics outlined above show that it is challenging to manufacture samples with different twist angles, all with sufficiently small disorder, in order to study the dependence of the IX localization and transport on the twist angle and, in turn, on the moiré superlattice period. Consequently, this remains the subject for future works.

### Supplementary Notes 2: Optical measurements

In the cw experiments, excitons were generated by a cw Ti:Sapphire laser with tunable excitation energy or a cw HeNe laser with excitation energy  $E_{\text{ex}} = 1.96$  eV. Luminescence spectra were measured using a spectrometer with resolution 0.2 meV and a liquid-nitrogen-cooled CCD. The spatial profiles of IX luminescence vs.  $x$  were obtained from the luminescence images detected using the CCD. The signal was integrated from  $y = -0.5$  to  $y = +0.5 \mu\text{m}$ . Figure S3 shows a representative luminescence image. Figure S4 shows spectra for resonant and non-resonant excitation.

The IX luminescence kinetics was measured using a pulsed semiconductor laser with  $E_{\text{ex}} = 1.694$  eV nearly resonant to WSe<sub>2</sub> DX energy. The emitted light was detected by a liquid-nitrogen-cooled CCD coupled to a PicoStar HR TauTec time-gated intensifier.

The experiments were performed in a variable-temperature 4He cryostat. The sample was mounted on an Attocube xyz piezo translation stage allowing adjusting the sample position relative to a focusing lens inside the cryostat. All physical phenomena reported in the paper are reproducible after ca. 100 cooling down to 2 K and warming up to

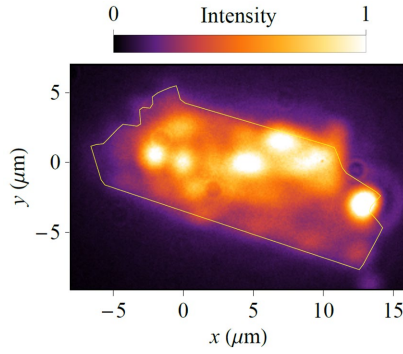


FIG. S3: IX luminescence image at  $P_{\text{ex}} = 0.2$  mW,  $T = 6$  K,  $E_{\text{ex}} = 1.623$  eV. The  $\sim 1.5$   $\mu\text{m}$  laser spot is centered at  $x = 0$ ,  $y = 0$ .

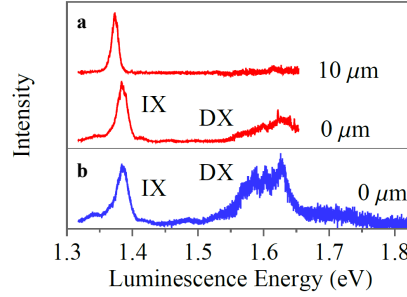


FIG. S4: The spectra for resonant [ $E_{\text{ex}} = 1.694$  eV, (a)] and non-resonant [ $E_{\text{ex}} = 1.96$  eV, (b)] excitation. The relative intensity of the higher-energy DX luminescence is lower for the resonant excitation, evidencing a lower temperature of the exciton system.  $P_{\text{ex}} = 0.2$  mW.  $T = 1.7$  K. The  $\sim 1.5$   $\mu\text{m}$  laser spot is centered at  $x = 0$ ,  $y = 0$ .

room temperature.

### Supplementary Notes 3: The drift-diffusion model of IX transport

This section outlines the drift-diffusion model describing classical diffusive IX transport [18–20]. Within this model, IX transport is described by the equation for IX density  $n$

$$\frac{\partial n}{\partial t} = \nabla [D\nabla n + \mu n \nabla(u_0 n)] + \Lambda - \frac{n}{\tau} \quad (1)$$

The first and second terms in square brackets in Eq. 1 describe IX diffusion and drift currents, respectively. The latter originates from the IX repulsive dipolar interactions and is approximated by the mean-field ‘plate capacitor’ formula for the IX energy shift with density  $\delta E = nu_0$ ,  $u_0 = 4\pi e^2 d_z / \epsilon$  [21]. The diffusion coefficient

$$D = D^{(0)} \exp[-U^{(0)} / (k_B T + nu_0)] \quad (2)$$

accounts for the temperature- and density-dependent screening of the long-range-correlated in-plane potential landscape by interacting IXs [18–20].  $D^{(0)}$  is the diffusion coefficient in the absence of in-plane potential.  $U^{(0)}/2$  is the amplitude of the in-plane potential.  $\mu$  is the IX mobility. The IX generation rate  $\Lambda$  has a profile of the laser excitation spot.  $\tau$  is the IX lifetime.

Both the IX-interaction-induced screening of in-plane potential and the IX-interaction-induced drift from the origin contribute to an enhancement of IX transport with increasing IX density  $n$ . In particular, within the classical drift-diffusion model [18–20], the enhancement of IX transport due to the IX-interaction-induced screening of in-plane potential is described by Eq. 2. Fitting the IX cloud expansion by  $R^2 \sim D^* \delta t$  probes the effective IX diffusion coefficient  $D^* = D + \mu nu_0$ , which includes both the diffusion and the drift due to the density gradient [22].  $\mu$  can be estimated

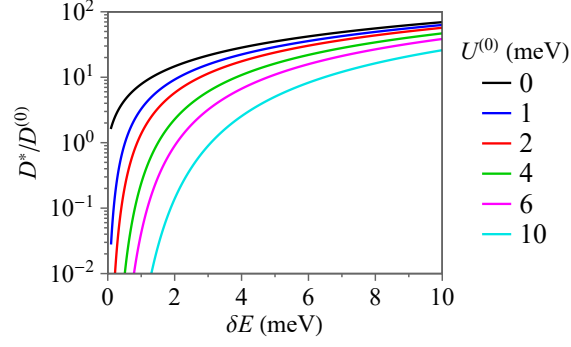


FIG. S5:  $D^*/D^{(0)}$  vs.  $\delta E$  for different  $U^{(0)}$ .  $T = 1.7$  K.

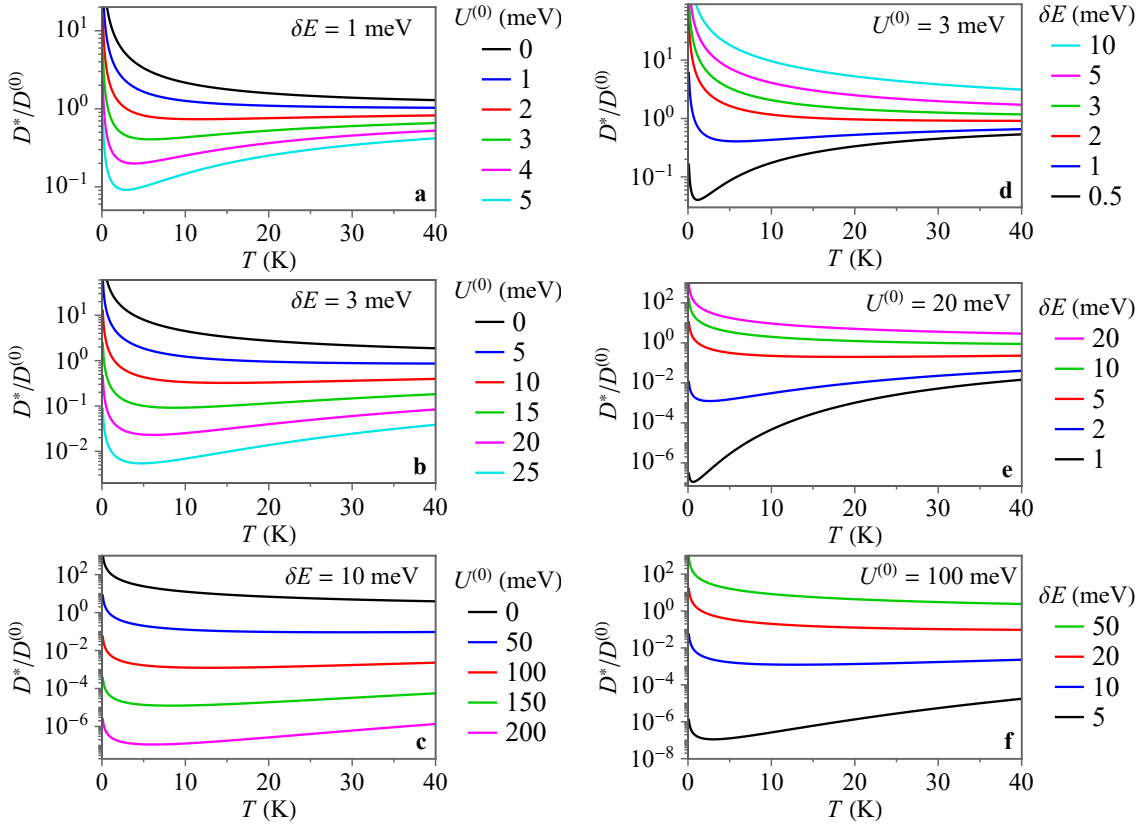


FIG. S6:  $D^*/D^{(0)}$  vs.  $T$  for different  $\delta E$  and  $U^{(0)}$ .

using the Einstein relation  $\mu = D/(k_B T)$ . Therefore, the enhancement of IX transport due to the IX-interaction-induced drift from the origin is described by the enhanced  $D^*$  (Eq. 3) [22]

$$D^* = D[1 + nu_0/(k_B T)] \quad (3)$$

Equations 2 and 3 show that within the classical drift-diffusion model [18–20], the IX transport should enhance with density for any amplitude of the in-plane potential and for any temperature. Figure S5 shows an enhancement of  $D^*$  with density for different  $U^{(0)}$ . The classical IX drift and diffusion [18–20] (Eqs. 1-3, Fig. S5) is inconsistent with the observed reduction of IX transport with density at high densities (Fig. 3a).

Equations 2 and 3 show that within the classical drift-diffusion model [18–20],  $D$  should increase with temperature for any  $U^{(0)}$  and the dependence of  $D^*$  on temperature is nonmonotonic (Fig. S6). Within this model,  $D^*$  increases with temperature when  $U^{(0)} > \delta E[1 + \delta E/(k_B T)]$ . The classical IX drift and diffusion model [18–20] (Eqs. 1-3, Fig. S6)

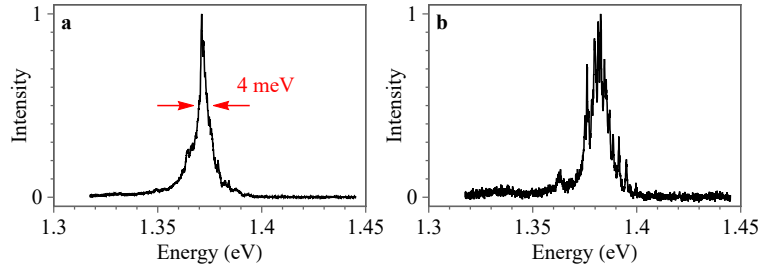


FIG. S7: (a) IX luminescence spectrum at a low IX density in the MoSe<sub>2</sub>/WSe<sub>2</sub> HS.  $P_{\text{ex}} = 5 \mu\text{W}$ ,  $T = 1.7 \text{ K}$ ,  $E_{\text{ex}} = 1.96 \text{ eV}$ . (b) IX luminescence spectrum showing sharp emission lines at lower IX densities in the MoSe<sub>2</sub>/WSe<sub>2</sub> HS.  $P_{\text{ex}} = 1 \mu\text{W}$ ,  $T = 1.7 \text{ K}$ ,  $E_{\text{ex}} = 1.689 \text{ eV}$ .

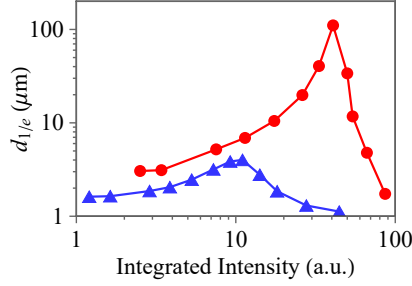


FIG. S8:  $d_{1/e}$  vs. integrated IX intensity in the entire MoSe<sub>2</sub>/WSe<sub>2</sub> HS. Excitation is either nonresonant ( $E_{\text{ex}} = 1.96 \text{ eV}$ , blue), or near resonant ( $E_{\text{ex}} = 1.623 \text{ eV}$ , red) to the DX.  $T = 6 \text{ K}$ .

is inconsistent with the observed vanishing of IX transport with temperature (Fig. 3b). Within the classical drift-diffusion model [18–20], the IX transport should enhance with the temperature for the strong moiré potentials [2, 3].

The drift-diffusion Eq. 1 can be supplemented by the thermalization equation, which describes heating of excitons by photoexcitation and cooling via interaction with phonons, and by including the HS in-plane potential in the drift term [19, 20]. In particular, the exciton thermalization can lead to the appearance of the inner ring in exciton luminescence patterns [19, 20]. The Einstein relation can be extended to the generalized Einstein relation  $\mu = D(e^{T_q/T} - 1)/(k_B T_q)$ , which gives  $\mu = D/(k_B T)$  for the classical drift and diffusion [18–20].

#### Supplementary Notes 4: IX interaction energies and the long-range IX transport

Below, we briefly discuss the IX interaction energies  $\delta E$  corresponding to the long-range IX transport. In GaAs HS, the strong enhancement of IX transport, the IX delocalization, is observed when the IX interaction energy becomes comparable to the amplitude of the in-plane potential, which is, in turn, comparable to the IX luminescence linewidth at low IX densities [23]. For the long-range IX transport in the MoSe<sub>2</sub>/WSe<sub>2</sub> HS, the IX interaction energy  $\delta E \sim 3 \text{ meV}$  (Fig. 2b). This value is comparable to the smallest IX linewidth  $\sim 4 \text{ meV}$  at low IX densities in the MoSe<sub>2</sub>/WSe<sub>2</sub> HS (Fig. S7a). However, the IX interaction energy  $\delta E \sim 3 \text{ meV}$  is significantly smaller than the predicted IX energy modulations in moiré superlattice potentials in MoSe<sub>2</sub>/WSe<sub>2</sub> HS that are in the range of tens of meV [2, 3]. This also shows that the IX transport in MoSe<sub>2</sub>/WSe<sub>2</sub> HS with the moiré superlattice potentials is distinct from the IX transport in GaAs HS. The classical drift and diffusion model [23] does not describe the quantum transport of repulsively interacting particles in periodic potentials. Sharp emission lines appear in the IX spectrum at lower densities (Fig. S7b). The sharp lines will be considered elsewhere.

#### Supplementary Notes 5: IX transport decay distance for nearly resonant excitation and nonresonant excitation

The nearly resonant excitation produces a higher IX density and, in turn, a stronger IX luminescence signal due to a higher absorption (Fig. 1). The higher IX densities can be also achieved by nonresonant excitation with

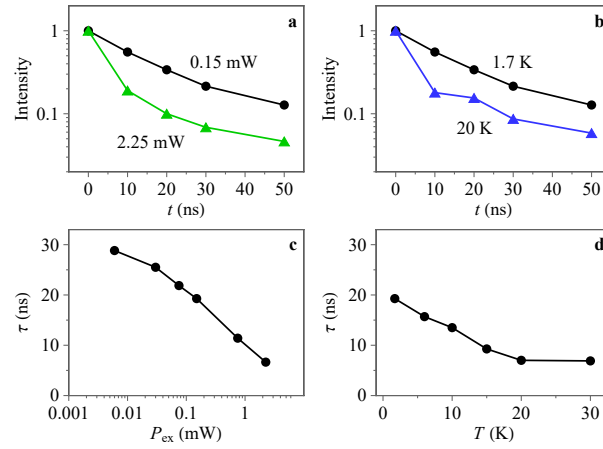


FIG. S9: IX decay kinetics. (a,b) Spatially integrated IX luminescence intensity vs. time for different  $P_{\text{ex}}$  (a) and temperatures (b). The times are given at the ends of the 10 ns signal integration windows. The excitation pulse ends at  $t = 0$ . (c,d) The IX lifetime  $\tau$  vs.  $P_{\text{ex}}$  (c) and vs. temperature (d).  $\tau$  is the initial decay time after the excitation pulse end.  $T = 1.7$  K (a,c),  $P_{\text{ex}} = 0.15$  mW (b,d). For all data,  $E_{\text{ex}} = 1.694$  eV.

higher excitation powers  $P_{\text{ex}}$ . Figure 2b shows that for the same  $\delta E$ , a much higher  $d_{1/e}$  is realized for the resonant excitation and that the strong enhancement of IX propagation originates from the suppression of localization and scattering of IXs, as described in the main text. This is confirmed by Fig. S8, which also compares the IX transport decay distances  $d_{1/e}$  for the nearly resonant and nonresonant excitations. Figure S8 shows that in the regime of the long-range IX transport at the nearly resonant excitation, for the same IX signal in the HS, achieved by a higher  $P_{\text{ex}}$  at nonresonant excitation,  $d_{1/e}$  is significantly longer in the case of the nearly resonant excitation. This indicates that the nearly resonant excitation is essential for the achievement of the long-range IX transport.

#### Supplementary Notes 6: IX decay kinetics

Figure S9 shows the IX luminescence decay kinetics after the laser excitation pulse is off. The IX decay times  $\tau$  (Fig. S9) are orders of magnitude longer than the DX decay times [24]. Both increasing  $P_{\text{ex}}$  (Fig. S9a,c) and temperature (Fig. S9b,d) lead to a reduction of  $\tau$ . This variation of  $\tau$  is rather weak and its effect on the IX transport variation is minor. For instance,  $\tau$  monotonically varies with  $P_{\text{ex}}$  (Fig. S9c) while the IX transport distance first increases and then reduces with  $P_{\text{ex}}$  (Fig. 3a) and the variation of  $\tau$  (Fig. S9c,d) is significantly smaller than the variation of  $d_{1/e}$  (Fig. 3).

#### Supplementary Notes 7: Rough estimates of the radiative and nonradiative lifetime variation with $P_{\text{ex}}$ and temperature

The IX radiative and nonradiative lifetimes,  $\tau_{\text{r}}$  and  $\tau_{\text{nr}}$ , can be roughly estimated from the measured IX total luminescence intensity  $I$  and decay time  $\tau$ . Figure S10 shows  $\tau_{\text{r}}$  and  $\tau_{\text{nr}}$  estimated using  $\tau_{\text{r}}^{-1} = (I/\Lambda)\tau^{-1}$  and  $\tau_{\text{nr}}^{-1} = \tau^{-1} - \tau_{\text{r}}^{-1}$ . Within this estimate, the IX luminescence kinetics is approximated as monoexponential. It is also assumed that there is no IX spatial escape from the system. This is approximated by integrating the IX luminescence signal over the heterostructure. For an estimate of the generation rate  $\Lambda$ , we use  $I_{\text{D}} = \alpha\Lambda$ , where  $I_{\text{D}}$  is the DX luminescence signal for the excitation at the MoSe<sub>2</sub> monolayer outside the heterostructure and  $\alpha$  is the quantum efficiency for this DX luminescence. Qualitatively similar variations of  $\tau_{\text{r}}$  and  $\tau_{\text{nr}}$  with  $P_{\text{ex}}$  and temperature are obtained for different values of  $\alpha$  (Fig. S10).

#### Supplementary Notes 8: IX transport kinetics

Figure S11 shows the kinetics of IX propagation from the excitation spot in the regime of long-range transport. The kinetics is measured during the rectangular-shaped laser excitation pulses with the duration 100 ns and period 300 ns. The 200 ns off time exceeds the IX lifetime (Fig. S9) and is sufficient for a substantial decay of the IX signal.

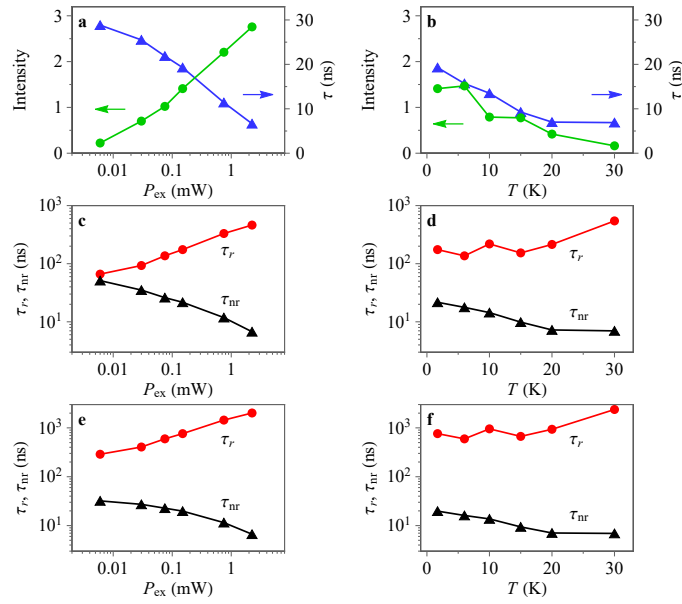


FIG. S10: Rough estimate of radiative and nonradiative lifetimes,  $\tau_r$  and  $\tau_{nr}$ . (a,b) Spatially integrated IX luminescence intensity  $I$  (green) and IX lifetime  $\tau$  (blue) vs.  $P_{ex}$  (a) and temperature (b).  $T = 1.7$  K (a),  $P_{ex} = 0.15$  mW (b), and  $E_{ex} = 1.694$  eV (a,b).  $\tau$  is the initial decay time after the excitation pulse end. (c-f) Estimated  $\tau_r$  and  $\tau_{nr}$  vs.  $P_{ex}$  (c,e) and temperature (d,f) for the quantum efficiency of DX luminescence in the MoSe<sub>2</sub> monolayer  $\alpha = 100\%$  (c,d) and 25% (e,f).

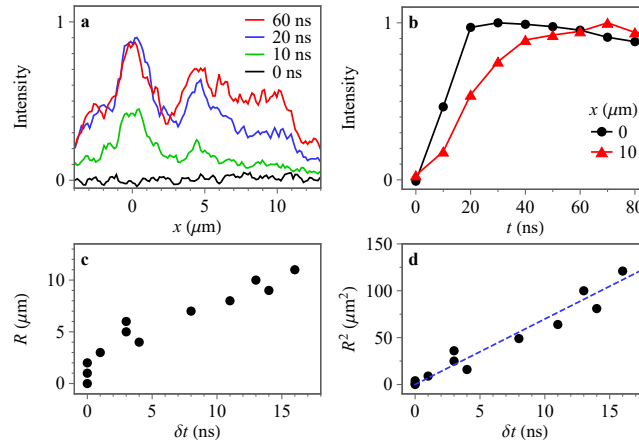


FIG. S11: IX transport kinetics. (a) IX luminescence profiles during the laser excitation pulse at different times. (b) Normalized IX luminescence intensity vs. time at different positions. (c)  $R$  vs.  $\delta t$ .  $\delta t$  is the time to reach 70% of the maximum intensity at distance  $R$  from the excitation spot relative to that time in the excitation spot. (d)  $R^2$  vs.  $\delta t$ . The dashed line is a fit to the data with  $D^* \sim R^2/\delta t \sim 70$  cm<sup>2</sup>/s.  $P_{ex} = 0.15$  mW,  $T = 1.7$  K, the times are given at the ends of the 10 ns signal integration windows, the excitation pulse starts at  $t = 0$ ,  $E_{ex} = 1.694$  eV, the  $\sim 2$   $\mu\text{m}$  laser spot is centered at  $x = 0$ .

The IX luminescence at locations away from the excitation spot is delayed in comparison to the IX luminescence in the excitation spot (Fig. S11a,b). The delay times  $\delta t$  for the IX cloud to expand to the locations separated by distance  $R$  from the origin allow estimating the IX transport characteristics. The substantial scattering of experimental points (Fig. S11c,d) does not allow distinguishing transport with nearly constant velocity  $R \propto \delta t$  from diffusive transport with  $R^2 \propto \delta t$ , therefore both approaches are probed. For the former approach, the estimated average velocity of the IX cloud expansion for the time range  $\Delta t = 1 - 20$  ns,  $v = \Delta R/\Delta t \sim 5 \times 10^4$  cm/s (Fig. S11c). For the latter approach, fitting the IX cloud expansion by  $R^2 \sim D^* \delta t$ , gives  $D^* \sim 70$  cm<sup>2</sup>/s (Fig. S11d). As described in Supplementary Notes 3, such fitting probes the effective IX diffusion coefficient  $D^* = D + \mu n u_0$ , which includes both the diffusion and the drift due to the density gradient [22]. The IX mobility  $\mu$  can be estimated using the Einstein relation  $\mu = D/(k_B T)$ ,



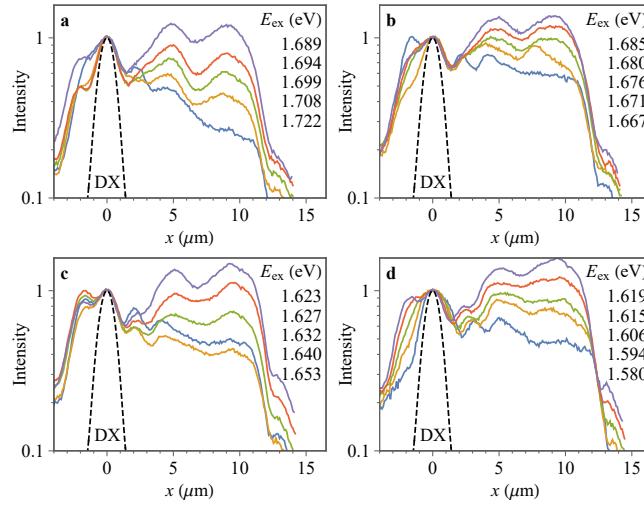


FIG. S12: Normalized IX luminescence profiles for different laser excitation energies  $E_{\text{ex}}$ . The dashed line shows the DX luminescence profile in the  $\text{WSe}_2$  monolayer, this profile is close to the laser excitation profile for a short DX propagation.  $P_{\text{ex}} = 0.2$  mW,  $T = 1.7$  K, the  $\sim 1.5$   $\mu\text{m}$  laser spot is centered at  $x = 0$ .

giving  $D^* = D[1 + nu_0/(k_B T)]$ . For  $nu_0 \sim 3$  meV,  $D^* \sim 70$   $\text{cm}^2/\text{s}$ , and  $T = 1.7$  K, this equation gives an estimate for the IX diffusion coefficient  $D \sim 4$   $\text{cm}^2/\text{s}$  and IX mobility  $\mu = D/(k_B T) \sim 3 \times 10^4$   $\text{cm}^2/(\text{eV s})$ . As outlined above, the observed IX transport is inconsistent with classical drift and diffusion, and these characteristics of IX transport are presented to allow a comparison with other studies of diffusive exciton transport.

#### Supplementary Notes 9: IX luminescence profiles for different laser excitation energies

Normalized IX luminescence profiles for different laser excitation energies  $E_{\text{ex}}$  are shown in Fig. S12. The long-range IX transport with high decay distances  $d_{1/e}$  is realized for  $E_{\text{ex}}$  close to the  $\text{MoSe}_2$  or  $\text{WSe}_2$  DX energy (Fig. 1). For some of the IX luminescence profiles no decay is observed within the HS. The data with the fit indicating  $d_{1/e} > 100$   $\mu\text{m}$  and showing no decay of the IX luminescence intensity with separation from the origin are presented in Fig. 1b by points on the edge.

\*equal contribution

#### References

- 
- [1] F. Withers, O. Del Pozo-Zamudio, A. Mishchenko, A.P. Rooney, A. Gholinia, K. Watanabe, T. Taniguchi, S.J. Haigh, A.K. Geim, A.I. Tartakovskii, K.S. Novoselov, Light-emitting diodes by band-structure engineering in van der Waals heterostructures, *Nat. Mater.* **14**, 301 (2015).
  - [2] H. Yu, G.-B. Liu, J. Tang, X. Xu, W. Yao, Moiré excitons: From programmable quantum emitter arrays to spin-orbit-coupled artificial lattices, *Sci. Adv.* **3**, e1701696 (2017).
  - [3] F. Wu, T. Lovorn, A.H. MacDonald, Theory of optical absorption by interlayer excitons in transition metal dichalcogenide heterobilayers, *Phys. Rev. B* **97**, 035306 (2018).
  - [4] Pasqual Rivera, Kyle L. Seyler, Hongyi Yu, John R. Schaibley, Jiaqiang Yan, David G. Mandrus, Wang Yao, Xiaodong Xu, Valley-polarized exciton dynamics in a 2D semiconductor heterostructure, *Science* **351**, 688 (2016).
  - [5] Luis A. Jauregui, Andrew Y. Joe, Kateryna Pistunova, Dominik S. Wild, Alexander A. High, You Zhou, Giovanni Scuri, Kristiaan De Greve, Andrey Sushko, Che-Hang Yu, Takashi Taniguchi, Kenji Watanabe, Daniel J. Needleman, Mikhail D.

- Lukin, Hongkun Park, Philip Kim, Electrical control of interlayer exciton dynamics in atomically thin heterostructures, *Science* **366**, 870 (2019).
- [6] Dmitrii Unuchek, Alberto Ciarrocchi, Ahmet Avsar, Kenji Watanabe, Takashi Taniguchi, Andras Kis, Room-temperature electrical control of exciton flux in a van der Waals heterostructure, *Nature* **560**, 340 (2019).
- [7] Dmitrii Unuchek, Alberto Ciarrocchi, Ahmet Avsar, Zhe Sun, Kenji Watanabe, Takashi Taniguchi, Andras Kis, Valley-polarized exciton currents in a van der Waals heterostructure, *Nature Nanotechnology* **14**, 1104 (2019).
- [8] Yuanda Liu, Kévin Dini, Qinghai Tan, Timothy Liew, Kostya S. Novoselov, Weibo Gao, Electrically controllable router of interlayer excitons, *Sci. Adv.* **6**, eaba1830 (2020).
- [9] Junho Choi, Wei-Ting Hsu, Li-Syuan Lu, Liuyang Sun, Hui-Yu Cheng, Ming-Hao Lee, Jiamin Quan, Kha Tran, Chun-Yuan Wang, Matthew Staab, Kayleigh Jones, Takashi Taniguchi, Kenji Watanabe, Ming-Wen Chu, Shangjr Gwo, Suenne Kim, Chih-Kang Shih, Xiaoqin Li, Wen-Hao Chang, Moiré potential impedes interlayer exciton diffusion in van der Waals heterostructures, *Sci. Adv.* **6**, eaba8866 (2020).
- [10] Zumeng Huang, Yuanda Liu, Kevin Dini, Qinghai Tan, Zhuojun Liu, Hanlin Fang, Jin Liu, Timothy Liew, Weibo Gao, Robust room temperature valley Hall effect of interlayer excitons, *Nano Lett.* **20**, 1345 (2020).
- [11] Long Yuan, Biyuan Zheng, Jens Kunstmann, Thomas Brumme, Agnieszka Beata Kuc, Chao Ma, Shibin Deng, Daria Blach, Anlian Pan, Libai Huang, Twist-angle-dependent interlayer exciton diffusion in WS<sub>2</sub>-WSe<sub>2</sub> heterobilayers, *Nat. Mat.* **19**, 617 (2020).
- [12] Zidong Li, Xiaobo Lu, Darwin F. Cordovilla Leon, Zhengyang Lyu, Hongchao Xie, Jize Hou, Yanzhao Lu, Xiaoyu Guo, Austin Kaczmarek, Takashi Taniguchi, Kenji Watanabe, Liuyan Zhao, Li Yang, Parag B. Deotare, Interlayer Exciton Transport in MoSe<sub>2</sub>/WSe<sub>2</sub> Heterostructures, *ACS Nano* **15**, 1539 (2021).
- [13] Jue Wang, Qianhui Shi, En-Min Shih, Lin Zhou, Wenjing Wu, Yusong Bai, Daniel Rhodes, Katayun Barmak, James Hone, Cory R. Dean, X.-Y. Zhu, Diffusivity Reveals Three Distinct Phases of Interlayer Excitons in MoSe<sub>2</sub>/WSe<sub>2</sub> Heterobilayers, *Phys. Rev. Lett.* **126**, 106804 (2021).
- [14] Daniel N. Shanks, Fateme Mahdikhanyarvejahany, Trevor G. Stanfill, Michael R. Koehler, David G. Mandrus, Takashi Taniguchi, Kenji Watanabe, Brian J. LeRoy, John R. Schaibley, Interlayer Exciton Diode and Transistor, *Nano Lett.* **22**, 6599 (2022).
- [15] Zhe Sun, Alberto Ciarrocchi, Fedele Tagarelli, Juan Francisco Gonzalez Marin, Kenji Watanabe, Takashi Taniguchi, Andras Kis, Excitonic transport driven by repulsive dipolar interaction in a van der Waals heterostructure, *Nature Photonics* **16**, 79 (2022).
- [16] Fedele Tagarelli, Edoardo Lopriore, Daniel Erkensten, Raúl Perea-Causín, Samuel Brem, Joakim Hagel, Zhe Sun, Gabriele Pasquale, Kenji Watanabe, Takashi Taniguchi, Ermin Malic, Andras Kis, Electrical control of hybrid exciton transport in a van der Waals heterostructure, *Nature Photonics*, <https://doi.org/10.1038/s41566-023-01198-w> (2023).
- [17] Matthew P. A. Fisher, Peter B. Weichman, G. Grinstein, Daniel S. Fisher, Boson localization and the superfluid-insulator transition, *Phys. Rev. B* **40**, 546 (1989).
- [18] A.L. Ivanov, Quantum diffusion of dipole-oriented indirect excitons in coupled quantum wells, *Europhys. Lett.* **59**, 586 (2002).
- [19] A.L. Ivanov, L.E. Smallwood, A.T. Hammack, Sen Yang, L.V. Butov, A.C. Gossard, Origin of the inner ring in photoluminescence patterns of quantum well excitons, *Europhys. Lett.* **73**, 920 (2006).
- [20] A.T. Hammack, L.V. Butov, J. Wilkes, L. Mouchliadis, E.A. Muljarov, A.L. Ivanov, A.C. Gossard, Kinetics of the inner ring in the exciton emission pattern in coupled GaAs quantum wells, *Phys. Rev. B* **80**, 155331 (2009).
- [21] D. Yoshioka, A.H. Macdonald, Double quantum well electron-hole systems in strong magnetic fields, *J. Phys. Soc. Jpn.* **59**, 4211 (1990).
- [22] C.J. Dorow, M.W. Hasling, E.V. Calman, L.V. Butov, J. Wilkes, K.L. Campman, A.C. Gossard, Spatially resolved and time-resolved imaging of transport of indirect excitons in high magnetic fields, *Phys. Rev. B* **95**, 235308 (2017).
- [23] M. Remeika, J.C. Graves, A.T. Hammack, A.D. Meyertholen, M.M. Fogler, L.V. Butov, M. Hanson and A.C. Gossard, Localization-Delocalization Transition of Indirect Excitons in Lateral Electrostatic Lattices, *Phys. Rev. Lett.* **102**, 186803 (2009).
- [24] T. Korn, S. Heydrich, M. Hirmer, J. Schmutzler, C. Schüller, Low-temperature photocarrier dynamics in monolayer MoS<sub>2</sub>, *Appl. Phys. Lett.* **99**, 102109 (2011).